

# Inverse scattering with a parametrized spatial spectral volume integral equation for finite scatterers

**Citation for published version (APA):**

Eijsvogel, S., Dilz, R., & van Beurden, M. C. (2023). Inverse scattering with a parametrized spatial spectral volume integral equation for finite scatterers. *Journal of the Optical Society of America A, Optics, Image Science and Vision*, 40(9), 1797-1808. <https://doi.org/10.1364/JOSAA.498167>

**DOI:**

[10.1364/JOSAA.498167](https://doi.org/10.1364/JOSAA.498167)

**Document status and date:**

Published: 01/09/2023

**Document Version:**

Accepted manuscript including changes made at the peer-review stage

**Please check the document version of this publication:**

- A submitted manuscript is the version of the article upon submission and before peer-review. There can be important differences between the submitted version and the official published version of record. People interested in the research are advised to contact the author for the final version of the publication, or visit the DOI to the publisher's website.
- The final author version and the galley proof are versions of the publication after peer review.
- The final published version features the final layout of the paper including the volume, issue and page numbers.

[Link to publication](#)

**General rights**

Copyright and moral rights for the publications made accessible in the public portal are retained by the authors and/or other copyright owners and it is a condition of accessing publications that users recognise and abide by the legal requirements associated with these rights.

- Users may download and print one copy of any publication from the public portal for the purpose of private study or research.
- You may not further distribute the material or use it for any profit-making activity or commercial gain
- You may freely distribute the URL identifying the publication in the public portal.

If the publication is distributed under the terms of Article 25fa of the Dutch Copyright Act, indicated by the "Taverne" license above, please follow below link for the End User Agreement:

[www.tue.nl/taverne](http://www.tue.nl/taverne)

**Take down policy**

If you believe that this document breaches copyright please contact us at:

[openaccess@tue.nl](mailto:openaccess@tue.nl)

providing details and we will investigate your claim.

# Inverse scattering with a parametrized spatial spectral volume integral equation for finite scatterers

S. EIJSVOGEL<sup>1,\*</sup>, R. J. DILZ<sup>1</sup>, AND M. C. VAN BEURDEN<sup>1</sup>

<sup>1</sup>Faculty of Electrical Engineering, Eindhoven University of Technology, 5612 AP Eindhoven, The Netherlands

\*Corresponding author: s.eijsvogel@tue.nl

Compiled September 5, 2023

In wafer metrology, the knowledge of the photomask together with the deposition process only reveals the approximate geometry and material properties of the structures on a wafer as a priori information. With this prior information and a parametrized description of the scatterers, we demonstrate the performance of the Gauss-Newton method for the precise and noise-robust reconstruction of the actual structures, without further regularization of the inverse problem. The structures are modeled as three-dimensional finite dielectric scatterers with a uniform polygonal cross-section along their height, embedded in a planarly layered medium. A continuous parametrization in terms of the homogeneous permittivity and the vertex coordinates of the polygons is employed. By combining the global Gabor frame in the spatial spectral Maxwell solver with the consistent parametrization of the structures, the underlying linear system of the Maxwell solver inherits all the continuity properties of the parametrization. Two synthetically generated test cases demonstrate the noise-robust reconstruction of the parameters by surpassing the reconstruction capabilities of traditional imaging methods at signal-to-noise ratios up to -3 dB with geometrical errors below  $\lambda/7$ , where  $\lambda$  is the illumination wavelength. For signal-to-noise ratios of 10 dB, the geometrical parameters are reconstructed with errors of approximately  $\lambda/60$  and the material properties are reconstructed with an error of around 0.03%. The continuity properties of the Maxwell solver and the use of prior information are key contributors to these results. © 2023 Optical Society of America

<http://dx.doi.org/10.1364/ao.XX.XXXXXX>

## 1. INTRODUCTION

Optical scatterometry is a non-destructive metrology technique for evaluating the manufacturing quality of semiconductor structures on a wafer [1]. This technique measures and analyses the electric fields reflected from these structures, to monitor changes in a structure's geometry and permittivity distribution. In the analysis, the fields reflected from a structure are compared to fields generated by a computational model acting as a function of the estimated spatial permittivity distribution [2]. Here, the estimated geometry and permittivity distribution is based on the photomask and the material deposition process. Therefore, the geometry and material properties of the structures on a wafer are approximately known beforehand, but not exactly due to process variations. To extract these aspects of the produced structures precisely, the estimated spatial permittivity distribution is adjusted such that it minimizes the differences between the measurements and the output of the computational model [3–6]. This is a so-called inverse scattering problem.

The underlying computational model influences the reconstruction accuracy: a first-order Born approximation is only capable of reconstructing target features larger than about one third

of a wavelength of the illumination source [Ch. 10, 7], whereas a full-wave Maxwell solver [8] with a priori information was shown to be capable of reconstructing details in the range of a tenth of this wavelength. This makes a full-wave Maxwell solver a key ingredient for solving inverse scattering problems. Luckily, there are several computationally efficient full-wave Maxwell solvers [9–12] that focus on the electric scattering from semiconductor structures on a wafer. In [9–12], these structures are modeled as three-dimensional (3D) finite dielectric scatterers embedded in a planarly layered background medium.

The full-wave Maxwell solver in [10] has been successfully used for inverse scattering problems in the optical spectrum [8, 13, 14], where a set of parameters is introduced to describe and reconstruct (parts of) the spatial permittivity distribution of the scatterers via a low-order representation. This results in a dimensionality reduction for the inverse scattering problem, which can eliminate the need for additional regularization strategies for controlling the ill-posedness of the inverse scattering problem [15]. Further, a parametrized representation of the spatial permittivity distribution of the scatterers enables a straight-forward sensitivity analysis via a Gauss-Newton method, to obtain the impact of variation per parameter onto the scattered fields, i.e.

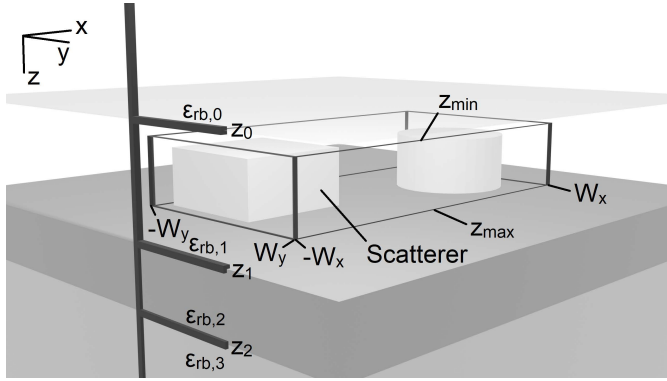


**Fig. 1.** Finite dielectric scatterers embedded in a single layer of the planarly layered background medium.

gradient information [15]. So, the parametrization of the spatial permittivity distribution for scatterers seems to be a viable approach for an accurate reconstruction process.

Unfortunately, there are parametrization pitfalls. First, it is possible that the introduced parameters only describe a part of the spatial permittivity distribution and, therefore, the misalignment between the measured and computed reflected fields can only be resolved as far as they have been parametrized. On the other hand, using too many parameters, i.e. overparametrization, can result in dependencies between the parameters, which leads to ill-conditioning of the Jacobian matrices within optimization problems [16]. In addition, overparametrization can also lead to overfitting [17]. Overall, it is important to keep track of the parameters. Fortunately, techniques such as the Morris method [18] gives insight into the impact of parameters, but at the cost of an increased computational workload. The second parametrization pitfall concerns the case where the parametrization of the permittivity distribution does not correspond with the discretization employed in the Maxwell solver, e.g. a discrete dipole approximation suffers from a discontinuous staircasing effect when the boundary of the geometry of a scatterer does not align with the axes of the coordinate system [19]. It limits the resemblance between the parametrized model and the intended spatial permittivity distribution and, therefore, the recovered parameters are expected to be of limited consistency [20]. Additional regularization strategies can aid the consistency of the recovered parameters [21]. However, it can increase the workload for the entire regularization strategy and it limits the reconstruction accuracy. Thus, a consistent parametrization of the spatial permittivity distribution of the scatterers is not straightforward and it is prone to the introduction of additional operations.

In the context of wafer metrology via optical scatterometry, we show that the continuous and consistent parametrization of the geometry and permittivity distribution of the scatterers by their polygon-shaped cross-sections provides access to analytic first-order partial derivatives of the scatterers per parameter in the spectral domain. This makes it possible to evaluate continuous variations of the parametrized permittivity distribution onto the scattered electric field via a Gabor-frame-based full-wave frequency-domain Maxwell solver, i.e. the spatial spectral volume integral equation (VIE) [9, 22]. Further, it enables a straightforward application of a parametrized Gauss-Newton method. Consequently, a Gauss-Newton inverse scattering method is constructed, which is based on the spatial spectral VIE with the

consistent parametrization of the scatterers and its associated first-order partial derivatives. This method does not exploit any form of regularization, other than the parametrization itself. As a result, we demonstrate a noise-robust and accurate parameter reconstruction in two test cases via this method: the reconstruction error for the geometrical parameters ranges from approximately  $\lambda/60$  to  $\lambda/7$  with  $\lambda$  the illumination wavelength, while working with signal-to-noise-ratio (SNR) levels from 10 dB to -3 dB, respectively. Further, the material parameters are obtained with less than 4.2% error with SNR levels up to -6 dB.

This paper is organized as follows. Section 2 briefly describes the key points of the spatial spectral VIE for the forward scattering problem, while Sec. 3 focuses on the Gabor-frame expansion of the analytic parametrization of the geometry and permittivity distribution for finite scatterers and the associated first-order partial derivatives. In Sec. 4, we describe key points of the inverse scattering framework. Two reconstruction test cases are discussed in Sec. 5, followed by the conclusions in Sec. 6.

## 2. FORWARD SCATTERING PROBLEM FORMULATION

### A. Geometrical description

Figure 1 displays the geometrical description employed in the spatial spectral VIE [p. 27, 22]. The background medium consists of  $N_L - 1$  homogeneous isotropic dielectric layers stacked in the  $z$ -direction, which is placed between two dielectric half-spaces. The relative permittivities of the layers are set by  $\epsilon_{rb,n}$  and the layer interfaces are located at  $z_n$  with the layer index  $n = 1, \dots, N_L - 1$ . We use index values  $n = 0$  and  $n = N_L$  for the top and bottom half-space, respectively. The simulation domain  $\mathcal{D}$  resides in only one layer and it is visualized by the black wire frame of size  $[-W_x, W_x] \times [-W_y, W_y] \times [z_{min}, z_{max}]$  that contains all scatterers.

### B. Spatial spectral VIE

The total electric field  $\mathbf{E}(\mathbf{x})$  is set as the superposition of the incident electric field  $\mathbf{E}^i(\mathbf{x})$  and the scattered electric field  $\mathbf{E}^s(\mathbf{x})$ , i.e.

$$\mathbf{E}(\mathbf{x}) = \mathbf{E}^i(\mathbf{x}) + \mathbf{E}^s(\mathbf{x}) \quad (1)$$

with the Cartesian coordinates  $\mathbf{x} = (x, y, z)$ . Here, we assume an  $e^{j\omega t}$  time dependence, where  $\omega$  is the angular frequency. The incident field originates from the top half-space in the form of a plane wave as

$$\mathbf{E}^i(\mathbf{x}) = \mathbf{E}^w e^{-j\mathbf{k}\cdot\mathbf{x}}, \quad (2)$$

where  $\mathbf{k} = (k_x, k_y, k_z)$  and  $\mathbf{E}^w$  is the amplitude vector of the plane wave. For the scattered electric field, the contrast function  $\chi(\mathbf{x}_t, z)$  is introduced that captures the finite dielectric scatterers embedded in layer  $n$ . The contrast function depends on a permittivity function  $\epsilon_r(\mathbf{x})$  that describes the permittivity distribution, including the dielectric scatterers, in layer  $n$  at position  $\mathbf{x}$ , such that we write the contrast function as

$$\chi(\mathbf{x}) = \frac{\epsilon_r(\mathbf{x})}{\epsilon_{rb,n}} - 1, \quad (3)$$

with  $\epsilon_{rb,n}$  the relative permittivity of the background in layer  $n$ . The contrast function is only non-zero at the location of scatterers. Thus, each scatterer is represented by a compact and finite permittivity distribution with respect to the background medium. Subsequently, the contrast current density is defined as

$$\mathbf{J}(\mathbf{x}_t, z) = j\omega\epsilon_0\epsilon_{rb,n}\chi(\mathbf{x}_t, z)\mathbf{E}(\mathbf{x}_t, z). \quad (4)$$

In the spatial spectral VIE, the scattered electric field is discretized simultaneously in the spatial and spectral domain. This way, the reflection and transmission coefficients of the layered background medium can be incorporated in a spectral Green function [23, 24]. To this end, we introduce the two-dimensional (2D) transverse Fourier transform  $f(\mathbf{k}_t)$  of  $f(\mathbf{x}_t)$  as

$$f(\mathbf{k}_t) = \mathcal{F}_{\mathbf{x}_t}[f(\mathbf{x}_t)](\mathbf{k}_t) = \iint_{\mathbb{R}^2} f(\mathbf{x}_t) e^{-j\mathbf{k}_t \cdot \mathbf{x}_t} d\mathbf{x}_t, \quad (5)$$

with  $\mathbf{x}_t = (x, y)$  and  $\mathbf{k}_t = (k_x, k_y)$ . The argument  $\mathbf{k}_t$  is used for functions residing in the spectral domain, while we use the argument  $\mathbf{x}_t$  for functions in the spatial domain. The operator  $\mathcal{F}_{\mathbf{k}_t}^{-1}[\dots]$  represents the inverse 2D transverse Fourier transformation. The scattered electric field in domain  $\mathcal{D}$  is represented as

$$\mathbf{E}^s(\mathbf{k}_t, z) = \int_{z_{\min}}^{z_{\max}} \mathcal{G}(\mathbf{k}_t, z|z') \cdot \mathcal{F}_{\mathbf{x}_t}[\mathbf{J}(\mathbf{x}'_t, z')](\mathbf{k}_t, z') dz' \quad (6)$$

with the spectral Green tensor  $\mathcal{G}(\mathbf{k}_t, z|z')$  containing the reflections and transmissions of the layered background medium as formulated in [25, 26]. By combining Eq. (1), Eq. (4), and Eq. (6), we write the spatial spectral VIE as

$$\mathbf{E}^i(\mathbf{k}_t, z) = \mathbf{E}(\mathbf{x}_t, z) - \mathcal{G}^{NF}[\chi(\mathbf{x}'_t, z')\mathbf{E}(\mathbf{x}'_t, z')](\mathbf{x}_t, z), \quad (7)$$

with a Green operator

$$\mathcal{G}^{NF}[\chi(\mathbf{x}'_t, z')\mathbf{E}(\mathbf{x}'_t, z')](\mathbf{x}_t, z) = \mathcal{F}_{\mathbf{k}_t}^{-1} \left[ \int_{z_{\min}}^{z_{\max}} \mathcal{G}(\mathbf{k}_t, z|z') \cdot \mathcal{F}_{\mathbf{x}_t}[\chi(\mathbf{x}'_t, z')\mathbf{E}(\mathbf{x}'_t, z')](\mathbf{k}_t, z') dz' \right](\mathbf{x}_t, z). \quad (8)$$

In the  $z$ -direction, this spatial spectral VIE is efficiently and recursively evaluated in a piecewise-linear discretization, while using the algorithm published in [27]. Further, Gabor frames are employed in the  $\mathbf{x}_t$ -plane for the expansion of the electric fields and the contrast current density function. Consequently, the contrast function becomes also expanded in a Gabor frame. The Gabor-frame expansion provides fast 2D transverse Fourier transformations by scalar multiplication applied to its expansion coefficients. In addition, Gabor frames exhibit exponential decay properties, see 3. Overall, the employed discretization scheme in the  $\mathbf{x}_t$ -plane and  $z$ -direction makes it possible to solve Eq. (7) by an iterative method such as BiCGstab( $\ell$ ) [28] and the pertaining matrix-vector products have a computational complexity of  $O(N \log N)$ , where  $N$  is the number of unknowns [9].

### 3. GABOR-FRAME EXPANSION OF A SCATTERER AND ITS PARTIAL DERIVATIVES

#### A. Gabor-frame expansion

As mentioned above, the spatial spectral VIE employs a Gabor-frame expansion in the transverse plane. Following [29], we describe a 2D Gaussian window function as

$$g(\mathbf{x}_t) = \sqrt{2} e^{-\pi \left( \frac{x^2}{\alpha_x^2} + \frac{y^2}{\alpha_y^2} \right)}, \quad (9)$$

to construct a spatial Gabor frame as

$$g_{\mathbf{mn}}(\mathbf{x}_t) = g(x - m_x \alpha_x X, y - m_y \alpha_y Y) e^{j\beta_x n_x K_x x + j\beta_y n_y K_y y}. \quad (10)$$

The parameters  $X = 2\pi/K_x$  and  $Y = 2\pi/K_y$  control the width of each Gaussian window function, while  $\alpha_x \beta_x < 1$

and  $\alpha_y \beta_y < 1$  are Gabor-frame oversampling parameters. The Gabor-frame parameter  $\alpha_x = \beta_x = \alpha_y = \beta_y$  are equal to  $\sqrt{2/3}$  in this work. The spatial shifts in the Gabor frames are described by the indices  $\mathbf{m} = (m_x, m_y)$ , whereas the modulation is set by  $\mathbf{n} = (n_x, n_y)$ . We continue with the spatial dual window function  $\eta(\mathbf{x})$  to construct spatial dual frames as

$$\eta_{\mathbf{mn}}(\mathbf{x}_t) = \eta(x - m_x \alpha_x X, y - m_y \alpha_y Y) e^{j\beta_x n_x K_x x + j\beta_y n_y K_y y}. \quad (11)$$

This function is synthesized as in [29] via a Moore-Penrose pseudo-inversion combined with the Gaussian window function as in Eq. (9). It provides dual frames with exponential decay. Other window functions for Eq. (9) are also possible and this choice influences the shape and decay of the dual window function [30, 31]. We define the Gabor expansion coefficients  $c_{\mathbf{mn}}$  of a square-integrable function  $f(\mathbf{x}_t)$  as

$$c_{\mathbf{mn}} = \int_{\mathbb{R}^2} f(\mathbf{x}_t) \eta_{\mathbf{mn}}^*(\mathbf{x}_t) d\mathbf{x}_t, \quad (12)$$

such that we represent  $f(\mathbf{x}_t)$  as

$$f(\mathbf{x}_t) = \sum_{\mathbf{m}} \sum_{\mathbf{n}} c_{\mathbf{mn}} g_{\mathbf{mn}}(\mathbf{x}_t). \quad (13)$$

The spectral Gabor frames are formed by the Fourier transform of Eq. (9). Therefore, the transformation between the spatial Gabor coefficients and spectral Gabor  $\hat{c}_{\mathbf{mn}}$  coefficients is provided by

$$c_{\mathbf{mn}} = \hat{c}_{\mathbf{nm}} e^{j2\pi(\alpha_x \beta_x m_x n_x + \alpha_y \beta_y m_y n_y)}. \quad (14)$$

The spectral dual window is also synthesized as in [29], which ensures that the spectral dual frames are also exponentially decaying functions.

#### B. Gabor coefficients of polygon-shaped scatterers

Here, each (finite) scatterer, occupying a domain  $\mathcal{D}_s$ , is assumed to be a locally homogeneous distribution with respect to the background medium at each  $z$ -sample, namely

$$\chi_s(\mathbf{x}_t, z) = \begin{cases} \varepsilon_r^s / \varepsilon_{rb,n} - 1 & (\mathbf{x}_t, z) \in \mathcal{D}_s \\ 0 & (\mathbf{x}_t, z) \in \mathbb{R}^3 \setminus \mathcal{D}_s, \end{cases} \quad (15)$$

with domain  $\mathcal{D}_s$  as a subdomain of  $\mathcal{D}$ . The scatterer's relative permittivity is described by  $\varepsilon_r^s$ . Index  $s = 1, \dots, S$  is used to fill simulation domain  $\mathcal{D}$  with all  $S$  scatterers. Unfortunately, the spatially discontinuous behavior of Eq. (15) induces a heavy computational workload for its spatial Gabor-frame expansion. The method in [32] overcomes this workload by computing the Gabor coefficients of the spectral equivalent of Eq. (15) under the assumption that the geometry of a scatterer is described by a 2D polygon for its (uniform) cross-section at a fixed value of  $z$ . This yields exponential decay of the truncation error within the spectral Gabor-coefficient integrals, owing to the smoothness of the cross-section in the spectral domain. The 2D polygonal shape of a cross-section is defined by the spatial coordinates of its vertices  $\mathbf{x}_i^s = (x_i^s, y_i^s)$  for  $i = 1, 2, \dots, L_s$ , in a counter-clockwise direction [32, 33]. Independent of the Gabor-frame expansion, the spectral representation of a scatterer's contrast function Eq. (15) with polygonal cross-section is given by

$$\chi_s(\mathbf{k}_t, z) = -\chi_s^s \sum_{i=1}^{L_s} j(\mathbf{k}_t^v \cdot \mathbf{d}_i) \frac{e^{j\mathbf{k}_t \cdot \mathbf{x}_i^s} (e^{j\mathbf{k}_t \cdot \mathbf{d}_i} - 1)}{j(\mathbf{k}_t \cdot \mathbf{k}_t) [\mathbf{k}_t \cdot \mathbf{d}_i]}, \quad (16)$$

with  $\mathbf{k}_t^v = (-k_y, k_x)$ , line segments  $\mathbf{d}_i = \mathbf{x}_{i+1}^s - \mathbf{x}_i^s$ , and a contrast scalar  $\chi_s^s = \frac{\varepsilon_r^s}{\varepsilon_{rb,n}} - 1$ . This definition depends on line

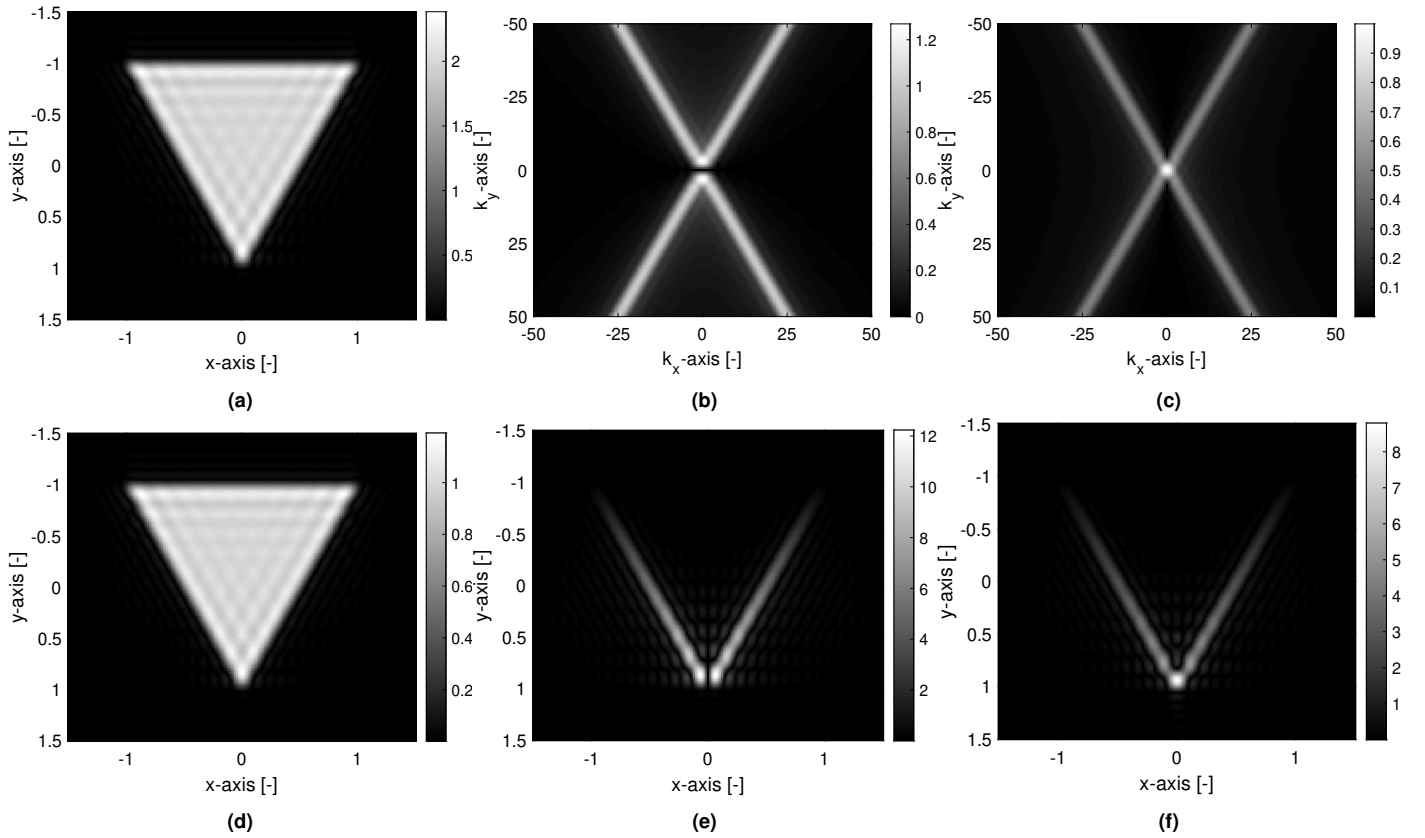


**Fig. 2.** The absolute amplitude of (a) a 2D cross-section with  $\chi_s^{sc} = 2$  expanded in Gabor frames. The spectral partial derivatives with respect to (b) the  $x$ -coordinate of the vertex  $\mathbf{x}_1 = (0, 1)$  and (c) the  $y$ -coordinate of the vertex  $\mathbf{x}_1$ . The absolute amplitude of the spatial partial derivative with respect to (d) the scaling factor  $\chi_s^{sc}$ , (e) the  $x$ -coordinate of the vertex  $\mathbf{x}_1$ , and (f) the  $y$ -coordinate of the vertex  $\mathbf{x}_1$ .

segments to connect the vertices  $\mathbf{x}_i^s$  and  $\mathbf{x}_{i+1}^s$ . Note that the  $\mathbf{x}_{i+1}^s$  for  $i = L_s$  needs to be set as  $\mathbf{x}_1^s$  to ensure a closed cross-section boundary. The spatial Gabor coefficients of a scatterer can be obtained by applying a Fourier transformation to the spectral Gabor coefficients as in Eq. (14). As a result of Eq. (16), the permittivity distribution of the scatterers is described by  $N_p$  parameters, gathered as the parameter vector

$$\begin{aligned} \bar{P}^T &= (p_1, \dots, p_{N_p}) \\ &= (x_1^1, y_1^1, \dots, x_{L_1}^1, y_{L_1}^1, \chi_1^{sc}, \dots, x_1^S, y_1^S, \dots, x_{L_S}^S, y_{L_S}^S, \chi_S^{sc}). \end{aligned} \quad (17)$$

A key advantage of this parametrization is that the permittivity distribution of scatterers is continuously differentiable with respect to the parameters.

### C. Gabor coefficients of a scatterer's partial derivatives

We continue by introducing the spectral definitions of the partial derivatives of a scatterer with respect to the parameter vector  $\bar{P}$ . The definitions of these partial derivatives can be classified into three types, namely partial derivatives with respect to a contrast scalar  $\chi_s^{sc}$ ,  $x$ -coordinate of a vertex, or  $y$ -coordinate of a vertex. The first type,  $\partial/\partial\chi_s^{sc}$ , contains the relative permittivity of a scatterer, while the other types,  $\partial/\partial x_i^s$  and  $\partial/\partial y_i^s$  with  $1 \leq i \leq L_s$ , describe the shape of a scatterer. The partial derivative with respect to the contrast scalar is obtained from Eq. (16) by setting the factor  $\chi_s^{sc}$  to 1. The partial derivative corresponding

to the  $x$ -coordinate of a vertex from a scatterer can be written as

$$\begin{aligned} \frac{\partial \chi_s}{\partial x_i^s}(\mathbf{k}_t, z) &= \frac{-j\chi_s^{sc}}{\mathbf{k}_t \cdot \mathbf{k}_t} \sum_{i=L-1}^L \left[ \frac{e^{j\mathbf{k}_t \cdot \mathbf{d}_i} - 1}{j[\mathbf{k}_t \cdot \mathbf{d}_i]} (-1)^{L-i} k_y + \right. \\ &\quad \left. j \frac{1 - e^{j\mathbf{k}_t \cdot \mathbf{d}_i} + e^{j(L-i)\mathbf{k}_t \cdot \mathbf{d}_i} j\mathbf{k}_t \cdot \mathbf{d}_i (\mathbf{k}_t^y \cdot \mathbf{d}_i) (-1)^{L+1-i} k_x}{(j[\mathbf{k}_t \cdot \mathbf{d}_i])^2} \right]. \end{aligned} \quad (18)$$

The partial derivative with respect to the  $y$ -coordinate of a vertex is obtained by replacing the variables  $k_y$  and  $k_x$  in the above equation by  $-k_x$  and  $k_y$ , respectively.

The result in Eq. (18) has term-wise removable singularities when  $\mathbf{k}_t \cdot \mathbf{d}_i \rightarrow 0$  and  $(\mathbf{k}_t \cdot \mathbf{d}_i)^2 \rightarrow 0$ . The singularity for  $\mathbf{k}_t = \mathbf{0}$  can be resolved by computing the partial derivative with respect to the corresponding  $x$ - or  $y$ -coordinate from [Eq. (8.7), 34], which is an equation to compute the area of a cross-section by using only its vertices. The corresponding expressions are

$$\left\{ \frac{\partial}{\partial x_i^s}, \frac{\partial}{\partial y_i^s} \right\} \chi_s(\mathbf{0}, z) = \frac{1}{2} \{ y_{i+1}^s - y_{i-1}^s, x_{i-1}^s - x_{i+1}^s \}. \quad (19)$$

Figure 2 contains an example of the three types of partial derivatives for a scatterer with a triangular cross-section. The subplots (b) and (c) are the Gabor-frame expanded version of Eq. (18) in the spectral domain, while subplots (d), (e), and (f) are the Gabor-frame expanded versions of the partial derivatives in the spatial domain. For this example, the Gabor-frame parameters are  $m_x, m_y, n_x, n_y \in \{-8, \dots, 8\}$  and  $X = Y = 1$ . The Gabor-frame expansion is used to provide an analytical

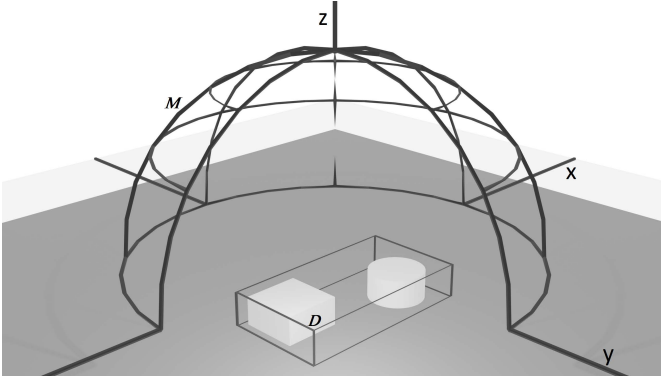


**Fig. 3.** An electromagnetic inverse scattering configuration with the domain  $\mathcal{M}$  and the domain  $\mathcal{D}$ .

link between the spatial and spectral domain via Eq. (14). We also note the appearance of the Gibbs phenomenon, due to the Dirac-delta behavior in the spatial domain in combination with a Gabor-frame expansion [9].

#### 4. INVERSE SCATTERING PROBLEM FORMULATION

##### A. Geometrical description

We base our reconstruction of the scatterers on the electric fields that are scattered upwards, see Fig. 3. These fields are detected on the surface of a half-sphere with a fixed radius, i.e. the (measurement) domain  $\mathcal{M}$ . This half-sphere is placed on top of layer 1 and, therefore, it is embedded in the top half-space. The distance between domain  $\mathcal{D}$  and  $\mathcal{M}$  is sufficiently large with respect to the wavelength to only consider the far-field response.

Here, the field components of the far-field response are approximated as plane waves with a direction indicated by spherical coordinates. Since the electric field of a plane wave is perpendicular to its propagation direction, only the transverse components  $E_\theta(\theta, \phi)$  and  $E_\phi(\theta, \phi)$  are computed on the surface of a half-sphere with a fixed radius  $r$ .

##### B. Near-to-far-field transformation

Now, we focus on linking the total electric  $\mathbf{E}(\mathbf{x})$  in domain  $\mathcal{D}$ , as obtained via the spatial spectral VIE, with the detected electric field in domain  $\mathcal{M}$  expressed in the spherical coordinate system. We first compute the scattered-field response from domain  $\mathcal{D}$  at the top of the layered background medium, i.e.  $z = z_0$ , by

$$\begin{aligned} \mathbf{E}^s(\mathbf{k}_t, z_0) &= \mathcal{G}^{FF}[\chi(\mathbf{x}'_t, z')\mathbf{E}(\mathbf{x}'_t, z')](\mathbf{k}_t, z_0) \\ &= \int_{z_{\min}}^{z_{\max}} \mathcal{G}(\mathbf{k}_t, z_0|z')\mathcal{F}_{\mathbf{x}'_t}[\chi(\mathbf{x}'_t, z')\mathbf{E}(\mathbf{x}'_t, z')](\mathbf{k}_t, z')dz'. \end{aligned} \quad (20)$$

Here, the 2D transverse Fourier transformation is without the complex-plane deformation employed in Eq. (8). Results from the spatial spectral VIE take the form of a planar plane-wave decomposition in the top half-space. The far-field response of Eq. (20) is obtained by only considering the propagating plane waves, which satisfy  $\sqrt{k_x^2 + k_y^2} \leq k_0$  with  $k_0$  the wavenumber in the top half-space. These propagating plane waves with their corresponding amplitudes in the spectral domain are transformed to a spherical far-field response via a spherical coordinate transformation combined with a phase-correction factor [35].

##### C. Inversion scheme

As mentioned in Sec. 1, optical scatterometry boils down to comparing measured fields reflected from the scatterers with the fields generated by a computational model. To this end, we introduce the cost functional  $F(\bar{\mathbf{P}}) \in \mathbb{R}^+$  to represent this difference between the measured (reference) far-field data and the far-field data from the spatial spectral VIE in measurement domain  $\mathcal{M}$  by a residual vector  $R(\bar{\mathbf{P}}) \in \mathbb{C}^{(2N_\theta N_\phi) \times 1}$  as

$$\begin{aligned} F(\bar{\mathbf{P}}) &= \|R(\bar{\mathbf{P}})\|_{\mathcal{M}}^2 \\ &= \sum_{h=1}^{N_\theta} \sum_{t=1}^{N_\phi} \sum_{u=1}^2 |E_u^{s,ref}(\theta_h, \phi_h, \mathbf{E}_t^i) - E_u^s(\theta_h, \phi_h, \mathbf{E}_t^i, \bar{\mathbf{P}})|^2. \end{aligned} \quad (21)$$

The  $\mathcal{M}$ -norm refers to the summation over the  $\theta$  ( $u = 1$ ) and  $\phi$  ( $u = 2$ ) polarization of the far-field data, the sample points  $\theta_h$  and  $\phi_h$  that represent the directions of scattering in domain  $\mathcal{M}$ , and the number of incident fields  $N_t$ . We use the variable  $N_\theta$  to express the number of sample points in domain  $\mathcal{M}$ . Ultimately, the aim is to minimize Eq. (21) by accurately reconstructing the geometry and permittivity distribution of the scatterers via the parameter vector  $\bar{\mathbf{P}}$  for all considered measured far-field responses. To this end, we employ a Gauss-Newton method [36][Sec. 6.5, 37], which iteratively minimizes the cost functional in Eq. (21) by determining the parameter values  $\bar{\mathbf{P}}$  that represent the geometry and permittivity distribution of the scatterers. The Gauss-Newton method starts with an initial guess of the parameter values  $\bar{\mathbf{P}}$ , which is iteratively adjusted as

$$\bar{\mathbf{P}}^m = \bar{\mathbf{P}}^{m-1} + \Delta\bar{\mathbf{P}}^m, \quad (22)$$

where  $m$  is the iteration index and  $\Delta\bar{\mathbf{P}}^m$  represents the update step. According to [36], this update step is obtained by solving the linear system

$$\mathbf{A}^m \Delta\bar{\mathbf{P}}^m = \mathbf{d}^m, \quad (23)$$

with the matrix  $\mathbf{A}^m \in \mathbb{C}^{N_p \times N_p}$  defined at row  $r$  and column  $c$  as

$$A_{r,c}^m = \left\langle \frac{\partial R}{\partial p_r}, \frac{\partial R}{\partial p_c} \right\rangle_{\mathcal{M}}, \quad (24)$$

and the vector  $\mathbf{d}^m \in \mathbb{C}^{N_p \times 1}$  at row  $r$  as

$$d_r^m = \left\langle \frac{\partial R}{\partial p_r}, R \right\rangle_{\mathcal{M}}. \quad (25)$$

Note that the brackets  $\langle \dots \rangle$  represent the inner product that induces the associated norm in Eq. (21). Further,  $\frac{\partial R}{\partial p_r}$  represents the partial derivative of the (vector) function  $R$ , defined in Eq. (21), with respect to a parameter  $p_r$ .

Consequently, we need to obtain the partial derivative of the function  $R$  for each parameter, such that we can employ the Gauss-Newton method. Since the reference data  $\mathbf{E}^{s,ref}$  is independent of the parameters, the partial derivative of the function  $R$  with respect to a parameter  $p$  can be written as

$$\begin{aligned} \frac{\partial R}{\partial p} &= \frac{\partial}{\partial p} \mathbf{E}^s(\mathbf{k}_t, z_0) = \frac{\partial}{\partial p} \mathcal{G}^{FF}[\chi(\mathbf{x}'_t, z')\mathbf{E}(\mathbf{x}'_t, z')] \\ &= \mathcal{G}^{FF} \left[ \left( \frac{\partial}{\partial p} \chi(\mathbf{x}'_t, z') \right) \mathbf{E}(\mathbf{x}'_t, z') + \chi(\mathbf{x}'_t, z') \frac{\partial}{\partial p} \mathbf{E}(\mathbf{x}'_t, z') \right]. \end{aligned} \quad (26)$$

The parameter  $p$  represents one of the  $N_p$  parameters in Eq. (17). A key point in Eq. (26) is that the parameter derivative is brought inside the operator  $\mathcal{G}^{FF}$ . We can actually compute all the terms of the parameter derivative. We have access to  $\chi(\mathbf{x}'_t, z')$  and

**Table 1.** The parameters defining the reference scatterers by their polygonal cross-section in accordance with Eq. (16) and their height in the  $z$ -direction in line with Eq. (6). The cross-sections  $\chi_1$  and  $\chi_2$  are used in the first test case, see Section 5.B. Cross-section  $\chi_3$  is used in the second test case, namely C.

	$x_1$ [nm]	$y_1$ [nm]	$x_2$ [nm]	$y_2$ [nm]	$x_3$ [nm]	$y_3$ [nm]	$x_4$ [nm]	$y_4$ [nm]	$\chi_s^{sc,SUT}$ [-]	$z_{min}$ [nm]	$z_{max}$ [nm]
$\chi_1$	-600	-1230	600	-1230	600	-30	-600	-30	0.2	0	150
$\chi_2$	-1200	30	1200	30	1200	1230	1230	-1230	0.3	0	150
$\chi_3$	-250	-500	250	-500	0	500	-	-	0.25	0	120

**Table 2.** The incident field angles given the spherical coordinates  $\theta$  and  $\phi$  for the demonstrations.

	$(\theta, \phi)_1$	$(\theta, \phi)_2$	$(\theta, \phi)_3$	$(\theta, \phi)_4$
Test case 1	$(0^\circ, 0^\circ)$	$(0^\circ, 45^\circ)$	$(75^\circ, 0^\circ)$	$(63.6^\circ, 45^\circ)$
Test case 2	$(0^\circ, 0^\circ)$	$(0^\circ, 50^\circ)$	$(65^\circ, 0^\circ)$	$(70^\circ, 60^\circ)$

$\frac{\partial}{\partial p} \chi(\mathbf{x}'_t, z')$  owing to Eq. (16) and Eq. (18), respectively. Further, the spatial spectral VIE provides access to the total electric field  $\mathbf{E}(\mathbf{x}'_t, z')$ , see Eq. (7). The only missing component in Eq. (26) is the partial derivative of the total electric field with respect to the parameter. Since only the contrast function is parametrized, the missing partial derivative can be obtained by applying  $\partial/\partial p$  on Eq. (7), which gives

$$\mathcal{G}^{NF} \left[ \left( \frac{\partial}{\partial p} \chi(\mathbf{x}'_t, z') \right) \mathbf{E}(\mathbf{x}'_t, z') \right] (\mathbf{x}_t, z) = \frac{\partial}{\partial p} \mathbf{E}(\mathbf{x}_t, z) - \mathcal{G}^{NF} \left[ \chi(\mathbf{x}'_t, z') \frac{\partial}{\partial p} \mathbf{E}(\mathbf{x}'_t, z') \right] (\mathbf{x}_t, z). \quad (27)$$

This equation is of the same form as in Eq. (7) and therefore the spatial spectral VIE can be used to solve Eq. (27) for  $\frac{\partial}{\partial p} \mathbf{E}$ . Consequently, we compute the parameter derivatives without resorting to a finite-difference approach and the result therefore does not depend on a finite step size, see e.g. [Ch. 9, 38][39].

Regarding the outcome of the computations of the parameter derivatives, it is noteworthy that the peak amplitude of the partial derivatives of the scatterers with respect to their vertex coordinates are proportional to the vertex coordinates of the scatterers themselves, whereas the peak amplitude of the partial derivatives of the scatterer with respect to the contrast scalar remains equal to 1. These differences in peak amplitudes lead to an ill-conditioned matrix  $\mathbf{A}^m$ . Therefore, the partial derivatives of the scatterers with respect to the contrast scalars are scaled by  $1/\sqrt{XY}$ , since these quantities of the Gabor-frame expansion are typically around the same order of magnitude as the vertex coordinates of the scatterers.

## 5. PARAMETER RECONSTRUCTION RESULTS

### A. Implementation and computation details

The 3D spatial spectral VIE is used as the forward model within this frequency-domain inverse scattering framework. The accuracy of this method has been evaluated with several test cases concerning electromagnetic scattering by finite objects embedded in a layered background medium, see [9, 25, 26]. This VIE was developed in FORTRAN, and it is accessible via Python owing to a shared-object extension. The inversion algorithm, a Gauss-Newton method, was developed in Python. The entire

**Table 3.** The Gabor-Frame Parameters for the demonstrations.

	$X, Y$ [nm]	$m_x, m_y$ [-]	$n_x, n_y$ [-]
Test case 1	1200	$\{-4, \dots, 4\}$	$\{-7, \dots, 7\}$
Test case 2a	200	$\{-7, \dots, 7\}$	$\{-13, \dots, 13\}$
Test case 2b	650	$\{-4, \dots, 4\}$	$\{-7, \dots, 7\}$

inverse scattering framework is executed on a single machine, which uses an AMD 3700X processor with 8 cores in combination with 32 GB RAM.

For the upcoming two test cases, each incident field is considered as a single plane wave of unit amplitude originating from the top half-space. These plane waves are constructed by their incident angle in terms of  $\theta$  and  $\phi$  as denoted in [40][p. 17, 41] with the polarization angle  $\psi = 0$  and the 3D (effective) reflection coefficients of the layered background medium [25, 26, 42]. The spherical components of the reference far-field and 3D spatial spectral VIE far-field are sampled on a square  $(\cos(\phi) \cos(\theta), \sin(\phi) \sin(\theta))$ -grid. Both  $\theta$  and  $\phi$  are sampled, to obtain a stepsize of 0.04 for both  $\cos(\phi) \cos(\theta)$  and  $\sin(\phi) \sin(\theta)$ . In addition, the far-field response is evaluated on the  $(\cos(\phi) \cos(\theta), \sin(\phi) \sin(\theta))$ -grid with a numerical aperture (NA) of 0.85, which leads to  $N_h = 1425$  samples per spherical component of the far-field.

We use three error definitions to evaluate the reconstruction error for this inverse scattering problem. The first error monitors the progress of the cost functional in Eq. (21). We choose to show the progress of this cost functional in a normalized form, since the amplitudes of the electric fields are fairly small due to the (nanometer) size of the scatterers. The normalized cost functional is given by

$$L(\bar{P}) = \frac{\sum_{h=1}^{N_h} \sum_{t=1}^{N_t} \sum_{u=1}^2 |E_u^{s,ref}(\theta_h, \phi_h, \mathbf{E}_t^i) - E_u^s(\theta_h, \phi_h, \mathbf{E}_t^i, \bar{P})|^2}{\sum_{h=1}^{N_h} \sum_{t=1}^{N_t} \sum_{u=1}^2 |E_u^{s,ref}(\theta_h, \phi_h, \mathbf{E}_t^i)|^2}. \quad (28)$$

The second error is applied to the material properties of the scatterers and is defined as

$$E_{mat} = \sqrt{\frac{\sum_{s=1}^S |\chi_s^{sc,SUT} - \chi_s^{sc}|^2}{\sum_{s=1}^S |\chi_s^{sc,SUT}|^2}}, \quad (29)$$

where  $\chi_s^{sc,SUT}$  represents the contrast scalar of the scatterer(s) under test (SUT). The third error is applied to the geometric

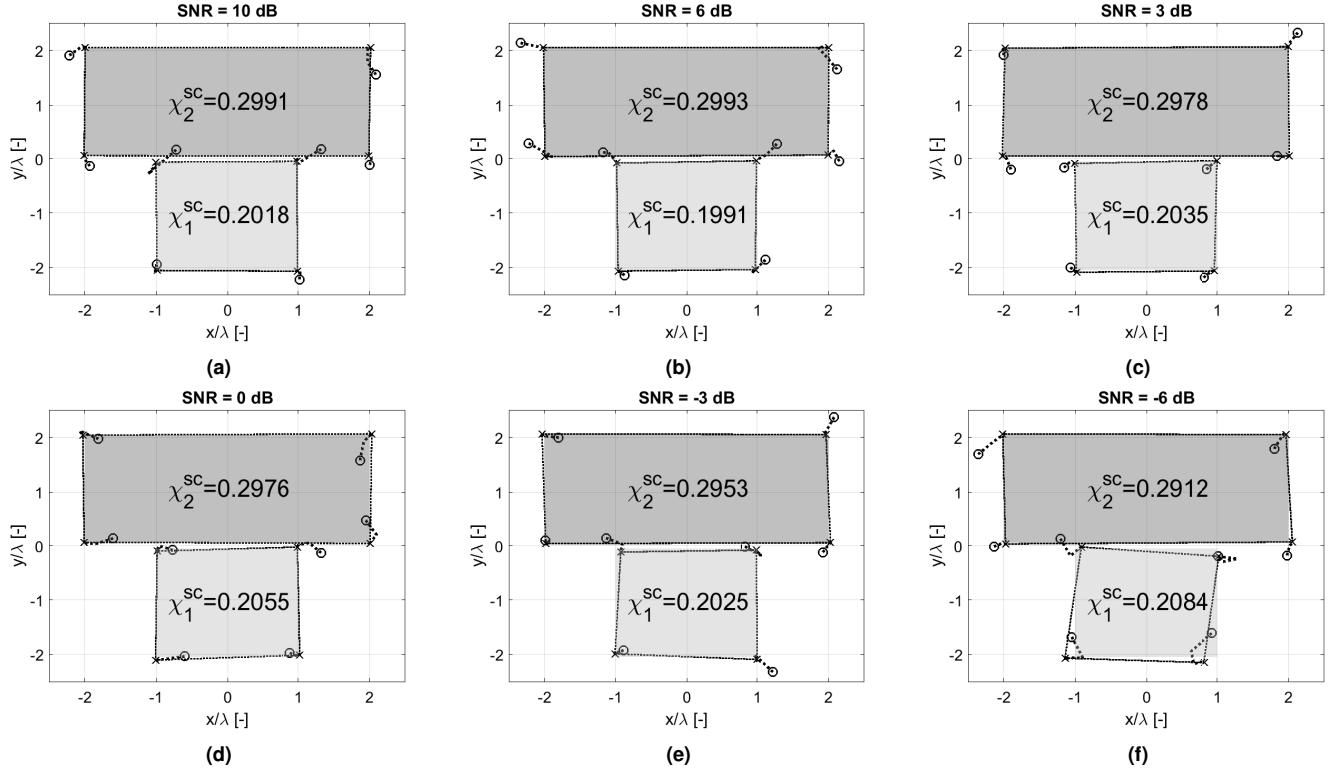


**Fig. 4.** The performance of the inverse scattering method per SNR level for the case consisting of two scatterers in vacuum. The circular markers display the initial guesses of the shape parameters and the cross markers, linked by dotted line segments, are the estimated shape parameters after the final Gauss-Newton update. The dashed line segments linking the circular markers and the cross markers represent the progression of the shape parameters during the Gauss-Newton iterations. The grey polygons are the actual scatterers as in Table 1. The  $\chi_s^{SC}$  values are the final estimations by the Gauss-Newton method.

properties of the scatterers and is defined as

$$E_{shape} = \frac{\sqrt{\sum_{s=1}^S \sum_{i=1}^{L_s} |x_i^{s,SUT} - x_i^s|^2 + |y_i^{s,SUT} - y_i^s|^2}}{\lambda}, \quad (30)$$

with  $\lambda$  the wavelength in the top half-space. These two types of parameter errors are explicitly decoupled, due to the differences in their order of magnitude in the optical-scatterometry setting. In addition, the performance of the inverse scattering method is evaluated by adding complex-valued Gaussian noise to each of the spherical components of the reference far-field data individually. This is done as follows. The average power in one of the two spherical components for a single far-field measurement is computed as  $\sigma^2 = (1/N_h) \sum_{h=1}^{N_h} |E_u(\theta_h, \phi_h, \mathbf{E}_t^i)|^2$ . This value is used to construct a Gaussian noise distribution, i.e.  $\mathcal{N}(\mu, 0.5\sigma^2) + j\mathcal{N}(\mu, 0.5\sigma^2)$  with  $\mu = 0$ . This noise distribution is then added as independent and identically distributed random variables to the far-field data samples of the pertaining spherical component.

There are two stopping criteria for the Gauss-Newton method. The first stopping criterion is that the minimum number of iterations is set to five, while the maximum number of iterations is set to a hundred. The second stopping criterion is linked to the steplength of the update of the vertex parameters, namely we stop when each vertex parameter satisfies

$$\frac{|p_r^m - p_r^{m-1}|}{\lambda} \leq \frac{1}{70}. \quad (31)$$

Here,  $p_r^m$  refers to one of the  $N_p$  parameters in the parameter

vector and  $m$  expresses the Gauss-Newton iteration count. The value  $1/70$  is heuristically chosen.

## B. Reconstructing multiple scatterers in vacuum

The first test case consists of two quadrilateral dielectric scatterers in vacuum. The contrast functions of these two scatterers  $\chi_1$  and  $\chi_2$  can each be described by a single cross-section for all considered  $z$ -samples. The exact vertex coordinates and contrast scalar of these two reference scatterers are listed in Table 1. In other words, these are the parameter values that we need to obtain as precisely as possible with the inverse scattering method. We explicitly use the fact that each of these two scatterers can be described by a single cross-section as a priori information. Therefore, this inverse scattering problem is described by eighteen parameters, namely eight vertex-coordinate parameters and one contrast scalar parameter per scatterer. Note that these two scatterers are separated by a gap of only 60 nm. The scatterers are illuminated by  $N_t = 4$  incident fields, where each plane wave has a wavelength of  $\lambda = 600$  nm. The incident angles are displayed in Table 2 under test case 1. The reference far-field response for this test case originates from CST Microwave Studio 2022 [43]. More specifically, its transmission line matrix (TLM) method is used, which is a time-domain method that approximates the Maxwell equations locally on a grid. This software package fits the geometric description in Fig. 3. For the spatial spectral VIE, the Gabor-frame expansion parameters used in domain  $\mathcal{D}$  can be found in Table 3 under test case 1. Further, 21 piecewise linear functions are used in the  $z$ -direction with  $\Delta_z = 7.5$  nm in domain  $\mathcal{D}$ . Each far-field response is measured

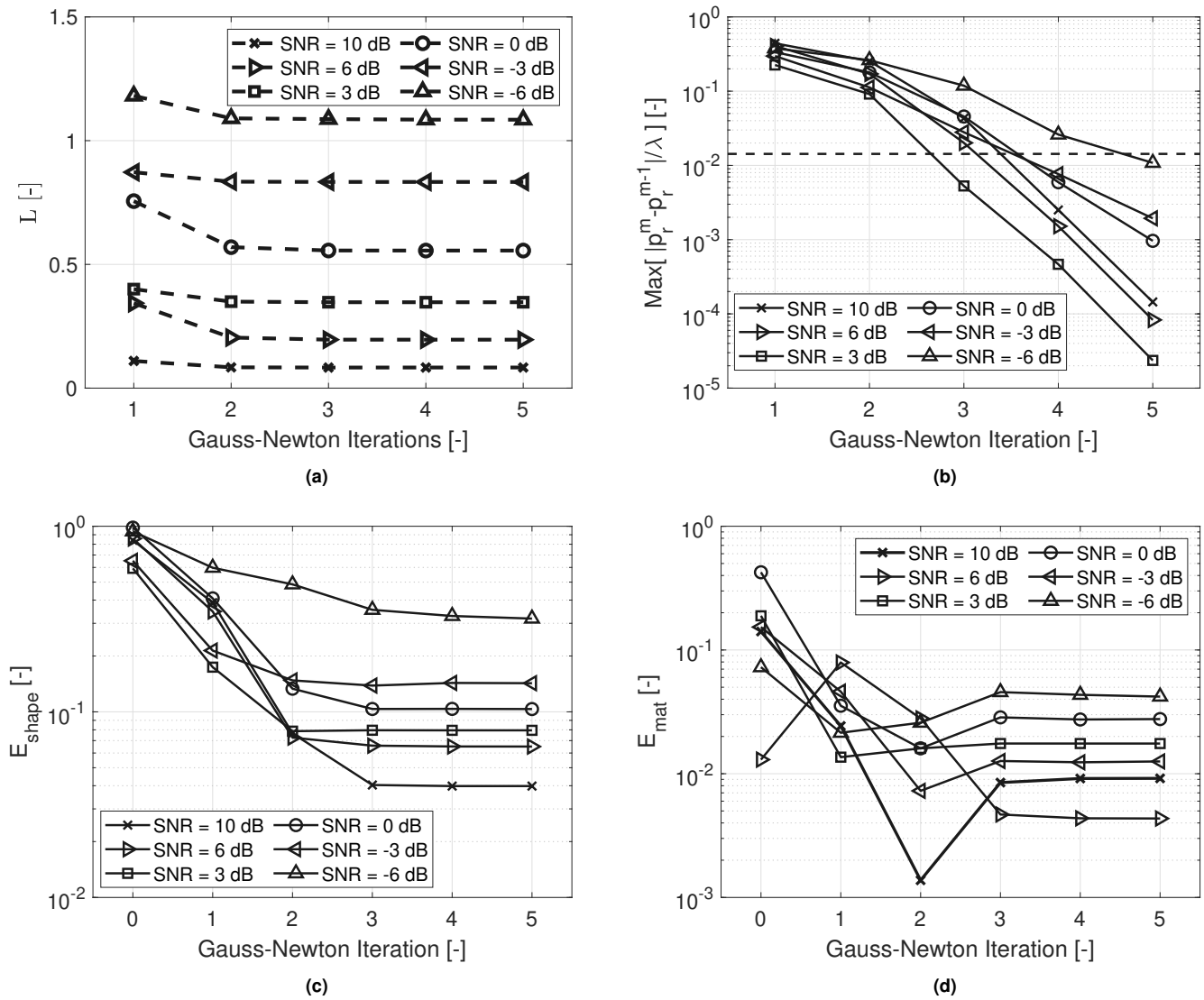


**Fig. 5.** (a) The performance of the inverse-scattering method per SNR in accordance to Eq. (28) for the case consisting of two scatterers in vacuum. (b) The observed maximum steplength in the vertex parameters during each iteration of the Gauss-Newton method per SNR. This is used to verify the stopping criterion as in Eq. (31), which is displayed by the dashed line. (c) The performance of the inverse scattering method per SNR in accordance to Eq. (29), while (d) displays the performance per SNR following Eq. (30).

at the boundary of a half-sphere centered at  $(x, y, z) = (0, 0, 0)$  with a radius of 1.2 m, which is an integer multiple of the wavelength. A key detail is that the far-field responses, as computed by the spatial spectral VIE, only differ by a relative  $\ell^2$ -error of approximately 0.01 from the reference far-field responses as computed by CST. Hence, the results of CST and the spatial spectral VIE method agree well.

Figure 4 shows the vertex positions of the quadrilaterals obtained by the Gauss-Newton method after five iterations (indicated by crosses) compared to the initial vertex positions (indicated by open circles) and the reference parameter values of the cross-sections, see the caption of the figure for a further explanation of the symbols. The initial vertex positions were obtained by applying a small random perturbation to the reference value of each parameter as in Table 1. This small random perturbation takes the form of a Gaussian distribution  $\mathcal{N}(0, 0.2\lambda)$  per vertex parameter, while each material parameter is subjected

to a perturbation of  $\mathcal{N}(0, 0.2\chi_s^{sc})$ . This means that we have approximate a priori information in the form of the approximate location, shape, and material properties of the scatterers. Figure 4 shows the reconstruction errors per SNR level, as defined in Eq. (29) and Eq. (30), for five iterations of the Gauss-Newton method. We note the following details from these two figures. First, Fig. 4 shows that the inverse-scattering framework is able to distinguish two scatterers for all tested SNR levels. This can be attributed to the parametrization, which forces the reconstruction of two independent quadrilateral cross-sections: the parameters of the large scatterer are completely independent with respect to the parameters of the smaller scatterer and vice versa. In addition, this independence between the parameters of the two scatterers also properly resolves a gap between the two scatterers, since the two scatterers do not morph into a single scatterer, nor do they overlap. Second, the reconstruction results regarding the vertex parameters for both scatterers achieve an er-

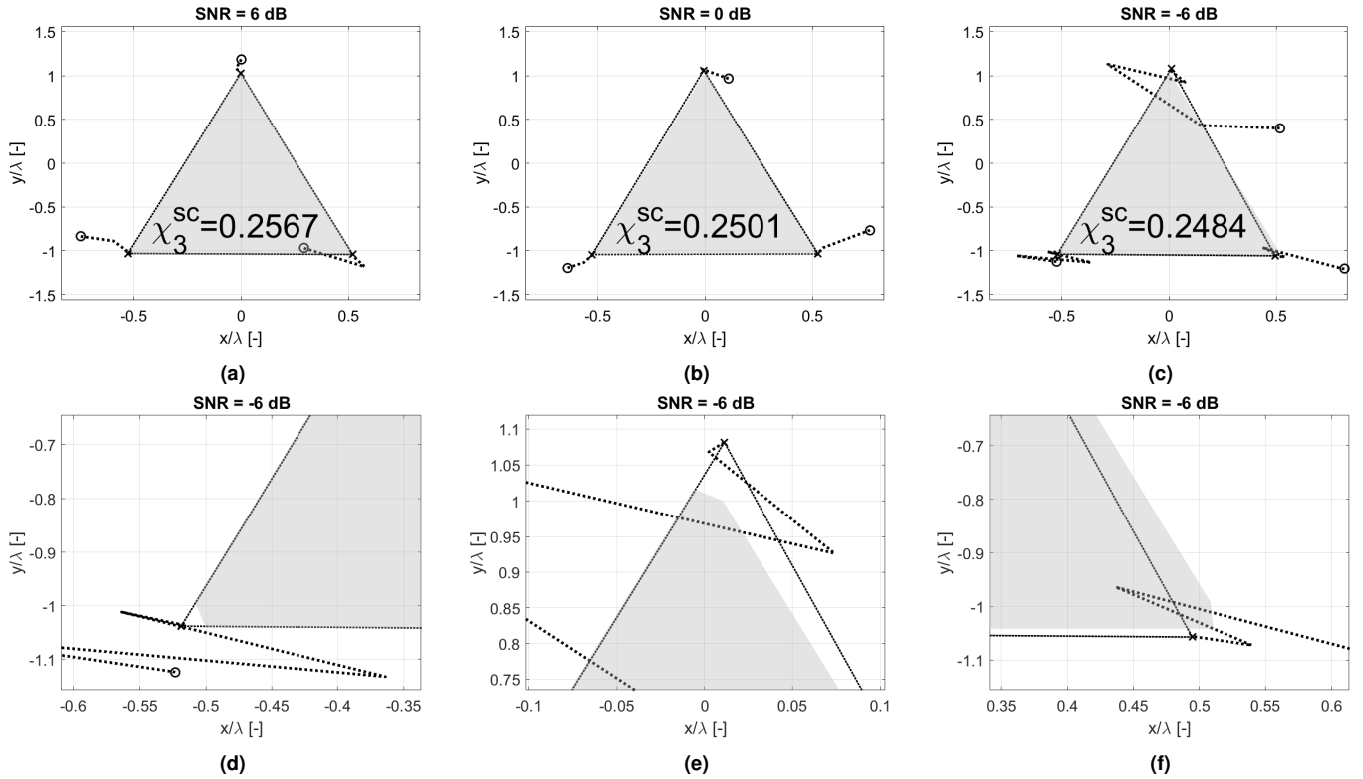


**Fig. 6.** The performance of the inverse-scattering method per SNR for the case consisting of a single scatterer embedded in a layered background medium. The circular markers display the initial guesses of the vertex parameters and the cross markers, linked by dotted line segments, are the estimated vertex parameters after the final Gauss-Newton update. The dashed line segments linking the circular markers and the cross markers represent the progression of the vertex parameters during the Gauss-Newton iterations. The grey polygons are the actual scatterers as in Table 1. The  $\chi_3^{sc}$  values are the final estimations by the Gauss-Newton method.

ror level of approximately 10% or less, for SNR levels up to 0 dB, as shown Fig. 5c. In other words, the reconstruction accuracy is at least a tenth of the wavelength for these SNR levels. The results in Fig. 4e, Fig. 4f, and Fig. 5c show that the reconstruction precision reduces an accuracy of approximately 31.8% for higher SNR levels. The reconstruction of the vertex parameters of the smaller scatterer becomes problematic at these SNR levels, whereas those of the larger scatterer are still quite accurately reconstructed. This is to be expected, since the large scatterer dominates the far-field response owing to its larger volume and higher permittivity in comparison to the smaller scatterer. Consequently, the far-field response of solely the smaller scatterer is the first contribution of the entire far-field response to drown in the noise. Third, the material properties are reconstructed with an error ranging from 0.4% up to 4.2% and, fourth, Fig. 5 shows that only three to five iterations are required for the Gauss-Newton method to obtain stable parameter values. A likely reason is that parametrization heavily reduces the solution space for this inverse scattering problem, since it only considers solutions in the form of two scatterers having four vertices each and an initial guess with an error in the form of Eq. (30) that is maximally a wavelength off. Our current implementation requires between 17 and 18 seconds on average to perform a full-wave solve of Eq. (7), in combination with the far-field transformation as in Eq. (20). This is also the case for a full-wave solve of Eq. (27) per parameter, while also subjecting its resultant to a far-field transformation as in Eq. (20). These computation times, in com-

bination with five iterations of the Gauss-Newton method, lead to a total computation time of approximately 7000 seconds. It might be possible to further reduce the total computation time by exploiting the adjoint method [Ch. 12, 44], such that derivative information can be computed in fewer steps. However, this is currently not available for the framework of the spatial spectral VIE. Overall, the parametrized permittivity distribution of two scatterers in vacuum are accurately reconstructed, even for low SNR levels.

### C. Object reconstruction in a layered medium

For the second demonstration, we look into the case of a triangular scatterer embedded in a layered background medium. The top half-space is vacuum with the layer interface  $z_0 = 0$  nm, while the bottom half-space, with its layer interface  $z_1 = 200$  nm, has a relative permittivity of 2. The background medium in which the scatterer is embedded has a relative permittivity of 3 and it is placed between the two half-spaces. To make the case more interesting, the triangular scatterer has its corner cut off, to resemble production errors. So, we try to reconstruct this scatterer as a triangular scatterer, while it is actually an irregular hexagonal scatterer. The triangular shape of the scatterer without cutting off the corners can be described by a single cross-section  $\chi_3$  for all considered  $z$ -samples and its details can be found in Table 1. The corner cuts are observable in Fig. 6d, Fig. 6e, and Fig. 6f. Since we assume to reconstruct a triangular scatterer, we describe this inverse-scattering problem by six vertex param-

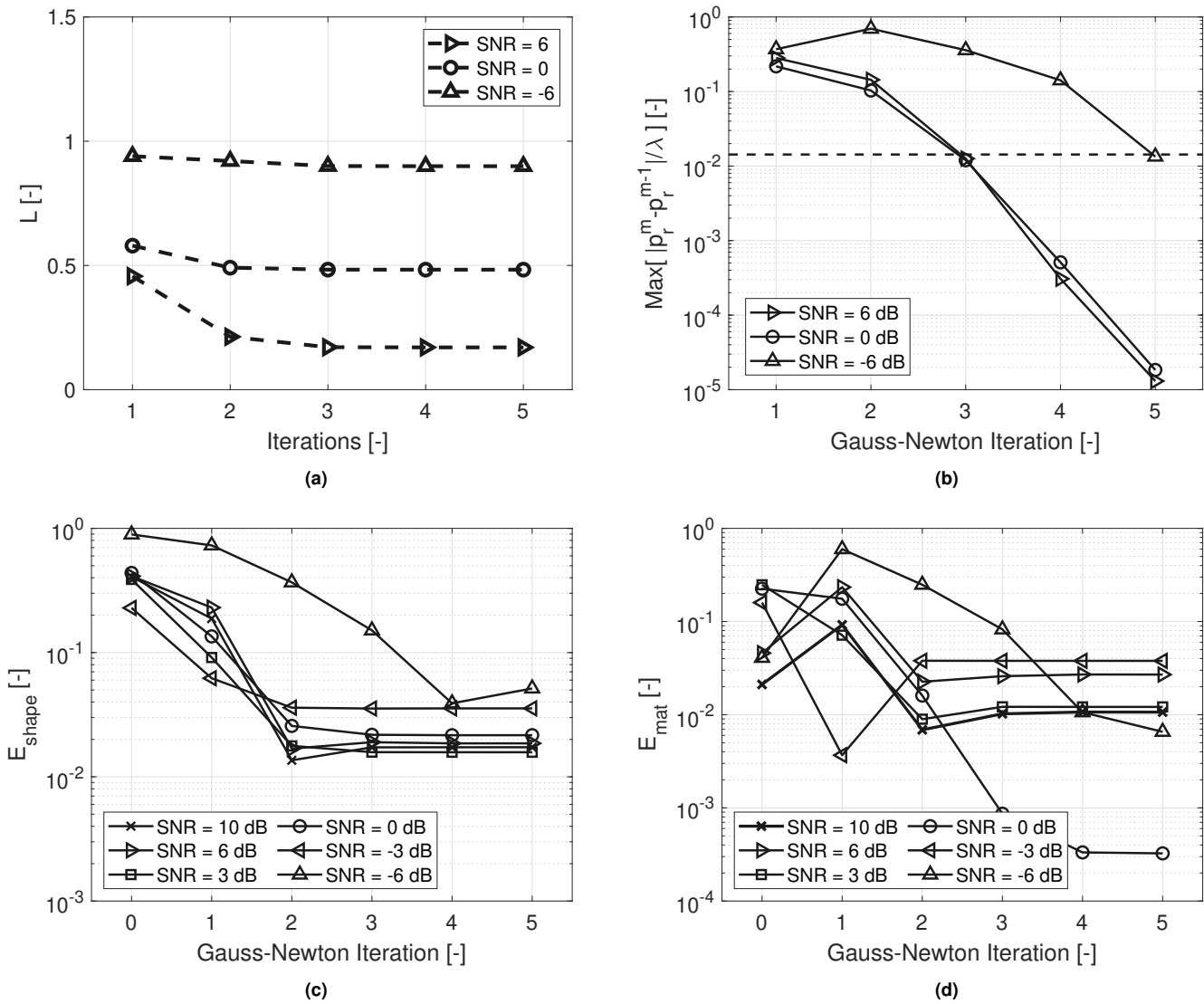


**Fig. 7.** (a) The performance of the inverse-scattering method per SNR in accordance to Eq. (28) for the case consisting of a single scatterer embedded in a layered background medium. (b) The observed maximum steplength in the vertex parameters during each iteration of the Gauss-Newton method per SNR. This is used to verify the stopping criterion as in Eq. (31), which is displayed by the dashed line. Note that only a part of the SNR settings are shown for the sake of readability in Figures (a) and (b). (c) The performance of the inverse scattering method per SNR in accordance to Eq. (29), while (d) displays the performance per SNR following Eq. (30).

ters and one material parameter. The scatterer is illuminated by  $N_t = 4$  incident plane waves with a wavelength of  $\lambda = 480$  nm in vacuum. The incident angles are displayed in Table 2 under test case 2. The far-field response is measured at the boundary of the half-sphere centered at  $(x, y, z) = (0, 0, 0)$  with a radius of 1.0 m. The Gabor-frame expansion settings for the reference far-field data is denoted as Test case 2a in Table 3, while the Gabor-frame settings for the test far-field data are indicated by Test case 2b. The number of piecewise linear functions in the  $z$ -direction for the reference far-field data  $E^{S,ref}$  and far-field data  $E^S$  are 24 and 5, respectively.

Figure 6 shows the reconstruction results for the irregular hexagonal scatterer approximated by a triangular cross-section for SNR levels 6, 0, and -6 dB. The details and symbols used this figure are explained in the caption. The accuracy of the recon-

struction is further illustrated and summarized in Fig. 7, which depicts a worst-case geometrical reconstruction error of approximately 5%, i.e. one-twentieth of the wavelength, for a SNR of -6 dB. Further, the worst-case error for the material properties is less than 4%. In addition, stable parameter values are already achieved after four Gauss-Newton iterations, which matches the number of iterations in the first demonstration for convergence. The performance in terms of the error measures in Eq. (29) and Eq. (30) in this test case is better than in the first test case. This is to be expected: this case only consists of a single scatterer with a total of seven parameters instead of two scatterers with a total of eighteen parameters, which makes the solution space of the second test case smaller than that of the first test case. For this specific triangular scatterer, the computation time for the five Gauss-Newton iterations is on average 756 seconds, since the

computation times for both Eq. (27) per parameter and Eq. (20) have been reduced to approximately 4 seconds. These computation times include the far-field transformation as in Eq. (20). The significant difference in computation time between the first and second demonstration can be attributed to the difference in the number of parameters and the number of samples in the  $z$ -direction.

## 6. CONCLUSION

We presented a Gauss-Newton inverse scattering method for the reconstruction of the geometry and the permittivity distribution of finite dielectric scatterers in vacuum or embedded in a layered background medium, in the presence of prior information. The dielectric scatterers were described by a continuous and consistent parametrization of their polygon-shaped cross-sections. This parametrization also gives access to the first-order partial derivatives per parameter. Further, a spatial spectral VIE was used in combination with this parametrization such that it was possible to continuously vary the geometry and the permittivity distribution of each scatterer by continuously varying its parameters. Two test cases were shown in which the Gauss-Newton method in combination with the spatial spectral VIE and the analytic parametrization was capable of accurate parameter reconstruction: the vertex parameters were reconstructed with errors of  $\lambda/60$  up to  $\lambda/7$ , with  $\lambda$  the illumination wavelength, at signal-to-noise ratios ranging from 10 dB to -3 dB, respectively. At a SNR of -6 dB, the material parameters were retrieved with an error of only 4.2%.

**Funding.** Dutch Research Council (NWO, project number: P16-08)

**Acknowledgments.** This work is part of the NWO-TTW Perspective project LINX with project number P16-08. Further, the authors would like to thank Meerten Versluis for his assistance in performing part of the reference calculations required for this work.

**Disclosures.** The authors declare no conflicts of interest.

**Data availability.** Data underlying the results presented in this paper are not publicly available due to project restrictions at this time but may be obtained from the authors upon reasonable request.

## REFERENCES

- C. J. Raymond, *Handbook of Silicon Semiconductor Metrology* (CRC press, 2001).
- F. Hagemann, T. Arens, T. Betcke, and F. Hettlich, "Solving inverse electromagnetic scattering problems via domain derivatives," *Inverse Probl.* **35** (2019).
- Y. Wang, H. Zhang, H. Guo, B. Wang, Y. Liu, X. He, J. Yu, H. Yi, and X. He, "Accurate and fast reconstruction for bioluminescence tomography based on adaptive newton hard thresholding pursuit algorithm," *J. Opt. Soc. Am. A* **39** (2022).
- M. Salucci, G. Oliveri, N. Anselmi, F. Viani, A. Fedeli, M. Pastorino, and A. Randazzo, "Three-dimensional electromagnetic imaging of dielectric targets by means of the multiscaling inexact-newton method," *J. Opt. Soc. Am. A* **34** (2017).
- J. Sugisaka, K. Harada, and K. Hirayama, "Inverse scattering algorithm for profile reconstruction of a buried defect beneath a dielectric rough surface based on the domain-boundary integral hybrid method," *J. Opt. Soc. Am. A* **39** (2022).
- N. Kumar, P. Petrik, G. K. P. Ramanandan, O. El Gawhary, S. Roy, S. F. Pereira, W. M. J. Coene, and H. P. Urbach, "Reconstruction of sub-wavelength features and nano-positioning of gratings using coherent Fourier scatterometry," *Opt. Express* **22**, 24678—24688 (2014).
- X. Chen, *Computational method for electromagnetic inverse scattering* (Wiley, 2018).
- M. Wurm, J. Endres, J. Probst, M. Schoengen, A. Diender, and B. Bodermann, "Metrology of nanoscale grating structures by uv scatterometry," *Opt. express* (2017).
- R. J. Dilz, M. G. M. M. van Kraaij, and M. C. van Beurden, "A 3D spatial spectral integral equation method for electromagnetic scattering from finite objects in a layered medium," *Opt. Quant. Electron.* **50** (2018).
- S. Burger, L. Zschidrich, J. Pomplun, and F. Schmidt, "Finite-element based electromagnetic field simulations: benchmark results for isolated structures," *Proc. SPIE 8880 Photomask Technol.* **8880** (2013).
- P. C. Chaumet, D. Sentenac, G. Maire, M. Rasedujjaman, T. Zhang, and A. Sentenac, "Ifdda, an easy-to-use code for simulating the field scattered by 3D inhomogeneous objects in a stratified medium: tutorial," *J. Opt. Soc. Am. A* **38** (2021).
- R. Schmehl, B. M. Nebeker, and E. D. Hirtleman, "Discrete-dipole approximation for scattering by features on surfaces by means of a two-dimensional fast fourier transform technique," *J. Opt. Soc. Am. A* **14** (1997).
- N. Farchmin, M. Hammerschmidt, P. I. Schneider, M. Wurm, B. Bodermann, M. Bär, and S. Heidenreich, "Efficient Bayesian inversion for shape reconstruction of lithography masks," *J. Micro/Nanolithography, MEMS, MOEMS* **19** (2020).
- M. Hammerschmidt, M. Weiser, X. G. Santiago, L. Zschiedrich, B. Bodermann, and S. Burger, "Quantifying parameter uncertainties in optical scatterometry using bayesian inversion," *Model. Aspects Opt. Metrol.* (2017).
- A. Aghasi, M. Kilmer, and E. L. Miller, "Parametric level set methods for inverse problems," *SIAM journal on Imaging Sci.* **4**, 618–650 (2011).
- X. Xu, Y. Shen, Y. Chi, and C. Ma, "The power of preconditioning in overparameterized low-rank matrix sensing," *arXiv:2302.01186v1* (2023).
- X. Chen, Z. Wei, M. Li, and P. Rocca, "A review of deep learning approaches for inverse scattering problems," *Prog. Electromagn. Res.* **167**, 67–81 (2020).
- P. Ansuinelli, W. M. J. Coene, and H. P. Urbach, "Automatic feature selection in EUV scatterometry," *Appl. Opt.* **58**, 5916–5923 (2019).
- M. A. Yurkin and A. G. Hoekstra, "The discrete dipole approximation: An overview and recent developments," *J. Quant. spectroscopy & radiative transfer* **106** (2007).
- D. Barchiesi and T. Grosge, "Propagation of uncertainties and applications in numerical modeling," *J. Opt. Soc. Am. A* **34** (2017).
- S. Colburn and A. Majumdar, "Inverse design and flexible parameterization of meta-optics using algorithmic differentiation," *Commun. physics* **4** (2021).
- R. J. Dilz, "A spatial spectral domain integral equation solver for electromagnetic scattering dielectric layered media," Ph.D. thesis, Eindhoven university of technology (2017).
- K. Michalski and J. R. Mosig, "Efficient computation of sommerfeld integral tails-methods and algorithms," *J. Electromagn. Waves Appl.* (2016).
- K. Michalski and J. R. Mosig, "Multilayered media green's functions in integral equation formulations," *IEEE transactions on Antennas Propag.* (1997).
- R. J. Dilz and M. C. van Beurden, "An efficient complex spectral path formulation for simulating the 2D TE scattering problem in a layered medium using Gabor frames," *J. Comput. Phys.* **50**, 528—542 (2017).
- R. J. Dilz, M. G. M. M. van Kraaij, and M. C. van Beurden, "The 2D TM scattering problem for finite objects in a dielectric stratified medium employing Gabor frames in a domain integral equation," *J. Opt. society Am. A* **8**, 1315—1321 (2017).
- I. Gohberg and I. Koltracht., "Numerical solution of integral equations, fast algorithms and krein-sobolev equation," *Numer. mathematics* **47**, 237–288 (1985).
- G. L. G. Sleijpen and D. R. Fokkema, "BiCGstab( $\ell$ ) for linear equations involving unsymmetric matrices with complex spectrum," *Electron. Trans. Numer. Anal.* **1**, 11–32 (1993).
- M. Bastiaans, "Gabor's expansion and the Zak transform for continuous-time and discrete-time signals: Critical sampling and rational oversampling," (1995).

30. A. Janssen and P. Sondergaard, "Iterative Algorithms to Approximate Canonical Gabor Windows: Computational Aspects," *J. Fourier Analysis Appl.* **31**, 211–241 (2007).
31. T. Strohmer, "Approximation of Dual Gabor Frames, Window Decay, and Wireless Communications," *Appl. Comput. Harmon. Analysis* **11**, 243–262 (2001).
32. S. Eijsvogel, L. Sun, F. Sepehripour, R. J. Ditz, and M. C. van Beurden, "Describing discontinuous finite 3D scattering objects in gabor coefficients: fast and accurate methods," *JOSA A* **39**, 86–96 (2022).
33. M. C. van Beurden and I. D. Setija, "Local normal vector field formulation for periodic scattering problems formulated in the spectral domain," *J. Opt. Soc. Am. A* **34**, 224–234 (2014).
34. C. Yang, *Introduction to GIS programming and fundamentals with Python and ArcGIS* (CRC, 2017).
35. L. Novotny and B. Hecht, *Principles of Nano-Optics* (Cambridge University Press, 2012), 1st ed.
36. R. Fletcher, *Practical methods of optimization* (Wiley, 1987).
37. P. M. van den Berg, *Forward and Inverse Scattering Algorithms based on Contrast Source Integral Equations* (Wiley, 2021), 1st ed.
38. A. Kharab and R. B. Guenther, *An introduction to numerical methods: a MATLAB approach* (CRC press, 2019).
39. M. Boresta, T. Colombo, A. De Santis, and S. Lucidi, "A mixed finite differences scheme for gradient approximation," *J. Optim. theory applications* (2022).
40. W. C. Chew, *Waves and fields in inhomogeneous media* (IEEE Press, 1995).
41. M. G. M. van Kraaij, "Forward diffraction modelling : analysis and application to grating reconstruction," Ph.D. thesis, Eindhoven university of technology (2011).
42. J. R. Wait, *Electromagnetic Waves in Stratified Media* (Pergamon Press, 1970).
43. F. Hirtenfelder, "Effective antenna simulations using cst microwave studio," *Int. ITG Conf. on Antennas* p. 239 (2007).
44. K. C. Giannakoglou and D. I. Papadimitriou, *Optimization and Computational Fluid dynamics* (Springer, 2022).